A Three Component Self-Assembled Epitaxial Nanocomposite Thin Film

*Dong Hun Kim, Xue Yin Sun, Nicolas M. Aimon, Jae Jin Kim, Michael J. Campion, Harry L. Tuller, Lior Kornblum, Fred J. Walker, Charles H. Ahn, and Caroline A. Ross**

A self-assembled three phase epitaxial nanocomposite film is grown consisting of ≈3 nm diameter fcc metallic Cu nanorods within square prismatic SrO rocksalt nanopillars in a $Sr(Ti,Cu)O_{3-\delta}$ perovskite matrix. Each phase has an epitaxial relation to the others. The core–shell-matrix structures are grown on $SrTiO_3$ substrates and can also be integrated onto Si using a thin $SrTiO_3$ buffer. The structure is made by pulsed laser deposition in vacuum from a $SrTi_{0.75}Cu_{0.25}O_3$ target, and formed as a result of the limited solubility of Cu in the perovskite matrix. Wet etching removes the 3 nm diameter Cu nanowires leaving porous SrO pillars. The three-phase nanocomposite film is used as a substrate for growing a second epitaxial nanocomposite consisting of $CoFe_2O_4$ spinel pillars in a $BiFeO_3$ perovskite matrix, producing dramatic effects on the structure and magnetic properties of the $CoFe_2O_4$. This three-phase vertical nanocomposite provides a complement to the well-known two-phase nanocomposites, and may offer a combination of properties of three different materials as well as additional avenues for strain-mediated coupling within a single film.

1. Introduction

Functional oxides such as perovskite-related oxides are attractive for next generation energy storage, photovoltaic, sensor, and memory devices due to their versatile properties including superconductive, magnetoresistive, thermoelectric and magnetocaloric, ionic and semiconductive properties, and their magnetic, ferroelectric, piezoelectric, and multiferroic behaviors.[1–5] Nanocomposite oxides, with heterogeneous structures, can enable combinations of useful properties in one film, and such films can be formed by codeposition of two dissimilar phases. A notable example is the vertical nanocomposites formed from a spinel and a perovskite phase, such as $BiFeO_3$–$CoFe_2O_4$ grown on (001) $SrTiO_3$ which consist of columnar crystals of the spinel within a perovskite matrix, both epitaxial with the substrate. These have shown magnetism, ferroelectricity, and magnetoelectric coupling,[5–8] and, moreover, the locations of the spinel pillars on the substrate can be guided using a template.[12–14] The self-assembled films are conveniently grown using pulsed laser deposition (PLD) from a single target or by alternating deposition from two different targets. Nanocomposite films have also been produced consisting of metallic nanostructures in an oxide matrix, including Co_xNi_{1-x} alloy nanowires, Co nanocrystals, nanofibers, or Fe nanorods embedded in a CeO_2, TiO_2, perovskite or other oxide matrix.[15–19] For example, metallic Cu nanopillars or nanoparticles in an oxide matrix have been reported for plasmon resonance studies and for battery electrodes.[20–22]

The vertical nanocomposite films reported to date comprise two different phases, but additional functionalities and cross-coupling of properties may be possible in nanocomposites with more than two phases. Three-phase oxide nanocomposites consisting of La_2O_3, SrO, and Co_2O_3 were reported previously[23,24] but there has been no report on three-phase nanocomposites showing a vertically oriented epitaxial growth analogous to that seen in two-phase nanocomposites. Other examples of self-assembled oxide nanostructures include SrO_x and $(La,Sr)O_x$ nanodots at the interface of $Sr(Ti,Fe)O_3$ and $La_{0.7}Sr_{0.3}MnO_3$ thin films, which formed as a consequence of strain relaxation and electrostatic and elastic interactions,[25,26] and compositional heterogeneities which were found to develop in perovskite films due to cation size and charge effects.[27]

In this article, we describe the growth of a three-phase self-assembled epitaxial nanocomposite thin film, denoted nc-STCu (nanocomposite-STCu), consisting of metallic Cu nanorods surrounded by a rocksalt-structured SrO oxide shell within a matrix of a $Sr(Ti,Cu)O_{3-\delta}$ perovskite phase. We then discuss the formation of a nanoporous oxide film by

Prof. D. H. Kim, Dr. X. Y. Sun, Dr. N. M. Aimon, J. J. Kim, M. J. Campion, Prof. H. L .Tuller, Prof. C. A. Ross
Department of Materials Science and Engineering
Massachusetts Institute of Technology
Cambridge, MA 02139, USA
E-mail: caross@mit.edu

Prof. D. H. Kim
Department of Materials Science and Engineering
Myongji University
Yongin, South Korea

Dr. X. Y. Sun
School of Materials Science and Engineering
Harbin Institute of Technology
Harbin 150001, P.R. China

Dr. L. Kornblum, Dr. F. J. Walker, Prof. C. H. Ahn
Department of Applied Physics
Yale University
New Haven, CT 06520, USA

DOI: 10.1002/adfm.201500332

chemically etching the nc-STCu to remove the Cu. Chemical etching of oxide films and silicon to make nanoporous structures and nanotemplates has been commonly reported,[28–30] but in the present case the pores are defined by the locations of the Cu nanorods. Finally, the remaining porous film was used as a substrate on which a $BiFeO_3$–$CoFeO_4$ two-phase epitaxial perovskite-spinel nanocomposite was grown, illustrating the influence of the substrate surface on $BiFeO_3$–$CoFeO_4$ nanocomposite formation.[31]

2. Results and Discussion

The films were grown by PLD from a single $SrTi_{0.75}Cu_{0.25}O_3$ target in vacuum, on substrates of single crystal $SrTiO_3$ (STO), STO-buffered (001) Si, Si with yttrium stabilized zirconia/ceria buffer layers, or as-received Si. Most films were grown at a substrate temperature of 650 °C. Further details are given in the Methods section.

Figure 1a shows X-ray diffractometer (XRD) scans of 180 nm thick unetched and etched nc-STCu films on STO (001) substrates. Unetched nc-STCu shows a perovskite (002) peak around $2\theta = 45°$ and a metallic fcc Cu (002) peak around $2\theta = 50°$ (JCPDS #004-0836). A third phase, SrO, is also present based on microscopy and etching experiments (described below), but its X-ray peak was not visible.

The out-of-plane lattice parameter of the perovskite phase in unetched nc-STCu was $c_{STCu,unetch} = 3.952 \pm 0.003$ Å which is 1.2% bigger than that of bulk STO ($a_{bulk,STO} = 3.905$ Å). This is consistent with the presence of both Cu ions and oxygen vacancies in the oxide. The ionic radii of Ti^{4+}, Cu^{1+}, and Cu^{2+} are 0.61, 0.77, and 0.73 Å, respectively,[32] so Cu ions substituting for Ti expand the lattice and introduce oxygen vacancies for charge compensation. The out-of-plane lattice parameter of the

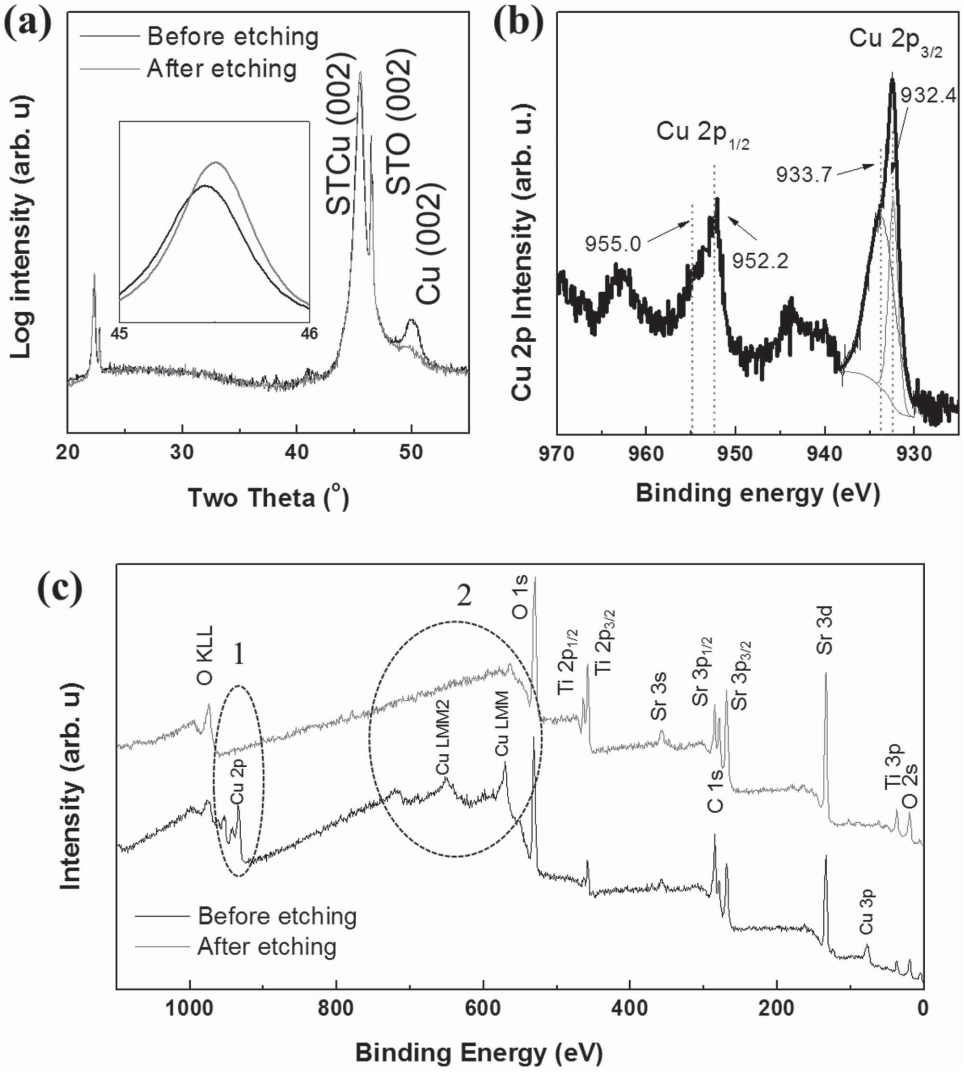

Figure 1. a) XRD patterns of unetched and etched STCu thin films deposited at 650 °C substrate temperature and in vacuum (2×10^{-6} Torr). Inset is a magnified XRD pattern around the nc-STCu perovskite (004) peak before and after etching. b) High resolution XPS spectrum of the Cu2p core level in an nc-STCu film grown at high vacuum. c) XPS survey scans of unetched and etched nc-STCu films showing removal of Cu by ammonium hydroxide etching.

metallic Cu was 3.665 ± 0.004 Å which is bigger than the bulk lattice parameter (3.615 Å), suggesting that the metallic Cu was strained in out-of-plane tension by its vertical epitaxy with the oxide matrix.

Figure 1b shows the X-ray photoelectron spectroscopy (XPS) spectrum of the core level Cu 2p in an unetched STCu film. Metallic Cu peaks (Cu $2p_{3/2}$ at 932.4 eV and Cu $2p_{1/2}$ at 952.2 eV) and divalent Cu^{2+} peaks at 933.7 and 955.0 eV[33,34] are shown accompanied by a broad satellite peak around 943 and 963 eV. The binding energies of univalent Cu^{+} and metallic Cu are close to each other[33,34] so it is difficult to distinguish them. However, the ratio of (Cu + Cu^{+}) to Cu^{2+} was 29.4: 70.6. Unlike STCu films grown in an oxygen atmosphere on a CeO_2/YSZ/Si substrate,[35] a Cu^{3+} peak was not detected.

To understand the spatial arrangement of the phases, **Figure 2**a,c shows the top view and 45° tilted scanning electron microscopy (SEM) images of an nc-STCu film with 30 nm thickness deposited at a vacuum of 2×10^{-6} Torr on an (001) STO substrate. Randomly distributed square crystallites with sides of length ≈10 nm are visible (Figure 2a) and these were confirmed to have a rod shape in the tilted image (Figure 2c). The square nanorods are bordered by four vertical {100} perovskite facets which have the lowest surface energy in perovskites[36,37] and the top of the rods protrudes ≈20 nm above the film surface. The [001] and [010] directions of STO and the perovskite matrix of the nc-STCu are drawn in Figure 2a.

Etching the sample in ammonium hydroxide led to changes in both the X-ray scan and the morphology. The metallic Cu peak intensity was reduced after etching showing that most of the metallic Cu was removed. The perovskite (002) peak of the etched sample shifted to a higher angle compared to the unetched sample, as shown in the inset of Figure 1a. The out-of-plane lattice parameter of the perovskite in the etched film was $c_{STCu,etch}$ = 3.948 ± 0.002 Å. The removal of metallic Cu was also confirmed from the XPS survey scan as shown in Figure 1c. After etching, the Cu2p peaks around 920–970 eV marked with circle 1 and the Auger Cu LMM triplet, which represents energy levels for the Cu Auger transitions between 550 and 750 eV marked with circle 2, disappeared. In XPS, no Cu peaks were observed after etching which suggests the ammonium hydroxide removed not only metallic Cu but also Cu^{2+} in the STCu matrix near the surface. This XPS data is consistent with the XRD results showing reduction of the Cu peak. Despite this, a small peak around 49.5° still remained suggesting some Cu was not etched, perhaps corresponding to Cu embedded deeper within the film.

SEM images of the etched sample (Figure 2b) showed the formation of pores (black spots) at the centers of the square nanorods, but the shells of the nanorods remained protruding above the sample surface even for long etch times (15 h). This implies that the nanorods were neither cupric oxide (CuO) nor cuprous oxide (Cu_2O) which are both etched by ammonium hydroxide. The inset in Figure 2b is a magnified top view SEM image of etched nc-STCu showing rods with ≈9 nm side length and pores of ≈3 nm diameter, and Figure 2d is a tilted image. However, the pores created from etching might not penetrate all the way through the film because it is difficult for the etchant to reach the bottom of the pores. In a 180 nm thick nc-STCu film (Figure S1, Supporting Information) similar rods of ≈10 nm side length were observed, which also formed pores after etching. Larger square facets were also seen but they did not etch.

To illustrate the integration of the nanocomposite on Si, nc-STCu was grown onto Si (100) coated with 8 nm STO by molecular beam epitaxy. In prior work we have shown that such substrates offer a good platform for growth of epitaxial perovskite and spinel nanocomposites.[31] Figure 2e,f shows tilted images of nc-STCu/8 nm STO/ Si before and after etching, and Figure S2e,f, Supporting Information, shows the top view images. The STO layer grew epitaxially with a 45° rotated cube-on-cube relationship to the Si substrate, and the nc-STCu grew on the STO/Si with similar morphology to its growth on single-crystal STO. The rods in the unetched STCu were tapered, and etching opened pores in their tops, marked with arrows in Figure 2f.

Cross-sectional transmission electron microscopy (TEM) characterization was conducted to investigate the detailed structure of the nanorods and nanopores. **Figure 3**a shows a low magnification cross-sectional TEM image of an unetched nc-STCu film on STO after focused ion beam (FIB) cutting along the [100] direction of the STO substrate demonstrating vertical nanorod growth. The rods were perpendicular to the film plane and showed larger diameter regions with a matchstick shape. Some rods grow all the way through while others terminated without reaching the surface.

A magnified cross-sectional TEM image of a rod containing dark matchstick shape phase (Figure 3b) shows different lattices. The TEM sample was cut parallel to the STO [100] axis, so the normal direction is [010] of STO and the film growth direction is [001]. The interplanar spacing of two perpendicular planes from the region surrounding the rod (Figure 3c) was 2.63 and 2.64 Å. These planes are consistent with the {002} planes of SrO which has a rock-salt structure (JCPDS #006-0520, a_{SrO} = 5.16 Å). We excluded the possibility that the core–shell structure consisted of metallic Cu surrounded by CuO, because CuO has a monoclinic structure and would not form perpendicular planes as observed here, and also excluded Cu_2O as the shell material because it is etched easily with ammonium hydroxide.

Figure 3d shows the central part of the rod. The interplanar spacing of two sets of planes making an angle of 55° with the surface of the STO substrate is 2.10 Å which corresponds to the (111) spacing of Cu, and the spacing of planes which are parallel to the STO (002) is 1.81 Å which corresponds to Cu (002). These observations are all consistent with the presence of metallic Cu, i.e., the Cu grows epitaxially with a 45° rotated cube-on-cube growth with respect to the STO substrate and the STCu film. The XRD phi scan did not show this relationship due to the low peak intensity from the small Cu nanorods. The perovskite STCu matrix phase was partly amorphized by the ion beam exposure during sample preparation, but the lattice fringe spacing marked in Figure 3b was 1.96 Å which is well matched with the strained (020) spacing of STCu with a zone axis of [010]. A schematic configuration of the orientations of the STCu, SrO, and Cu lattices along the [010] direction of the STO substrate is shown in Figure 3e. The interplanar spacing of (110) SrO is 3.73 Å which is intermediate between the out-of-plane lattice parameters of STCu (3.96 Å) and Cu (3.64 Å).

In a low magnification TEM image, it was hard to identify the effects of etching. In a higher magnification image the dark

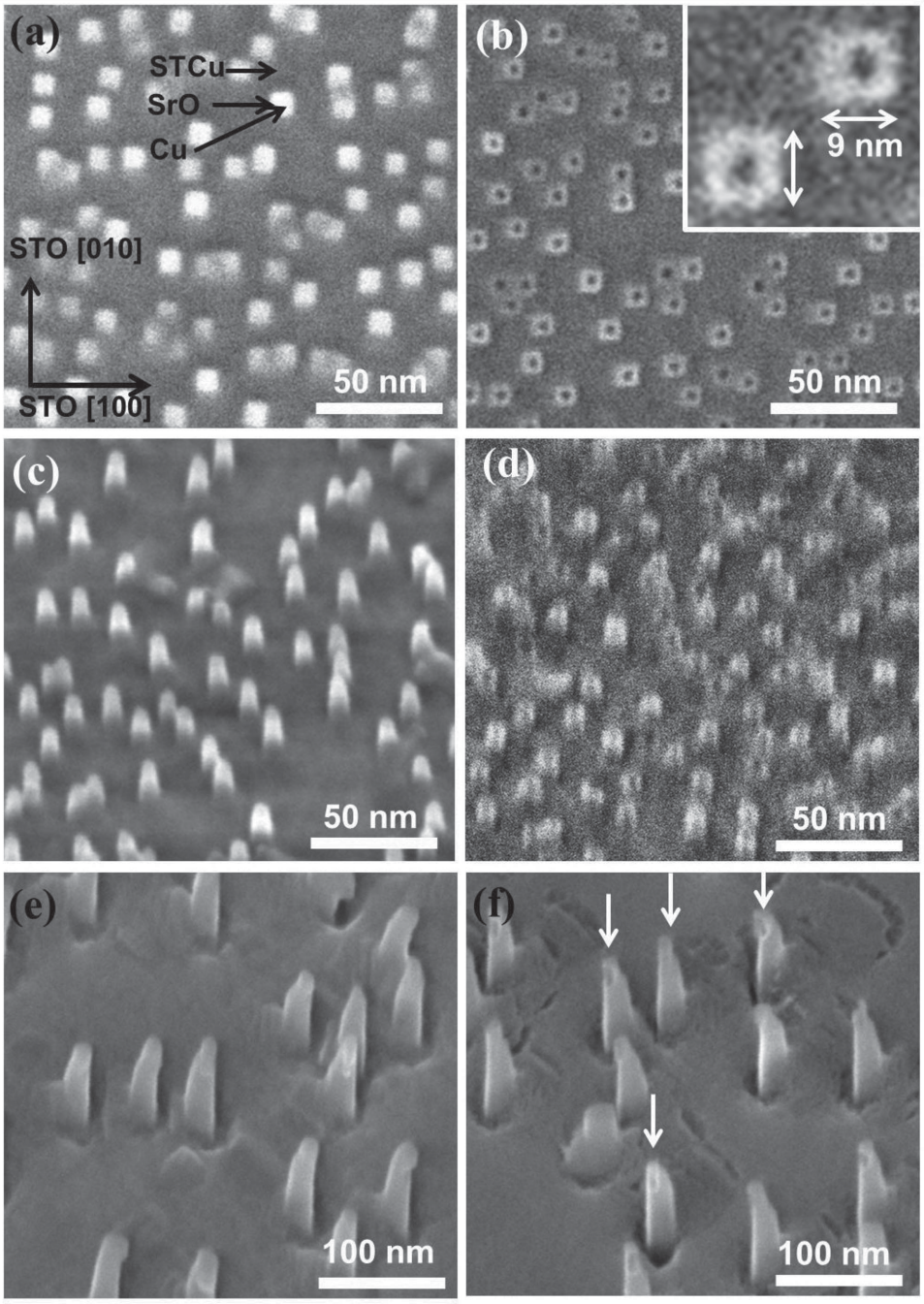

Figure 2. a) Top view SEM image of 30 nm thick nc-STCu film grown in vacuum and 650 °C substrate temperature. b) Top view SEM image of nc-STCu film etched in ammonium hydroxide for 3 hours. Inset is a magnified image of the pores in the SrO rods. 45° tilted SEM image of c) Cu nanorods and d) etched nanopores. 45° tilted SEM image of 180 nm thick nc-STCu films on STO/Si substrate e) before and f) after etching by ammonium hydroxide.

matchstick-shaped Cu phase was not observed, and the pores were not visible with TEM because of the projection of the adjacent SrO (not shown here).

The morphology of films grown on different substrates was also investigated. As mentioned above, nc-STCu on 8 nm STO/Si had a similar nanorod morphology compared to nc-STCu on STO (001) (Figure 2e,f and Figure S2e,f, Supporting Information). Nb-doped (001) STO (**Figure 4**a,b), (011) STO (Figure 4c), and (111) STO substrates (Figure 4d) also produced core–shell nanorods, with the Cu locations revealed by etching. On the Nb-doped (001) STO substrate the majority of rods grew along the [001] orientation but some rods grew with a [010] orientation as seen in the low magnification SEM image in the inset of Figure 4a. Compared to STO, the Nb-doped STO formed larger, less dense rods, which may indicate a difference in surface diffusivity as the film nucleates. In the (011) and (111) STO substrates, the

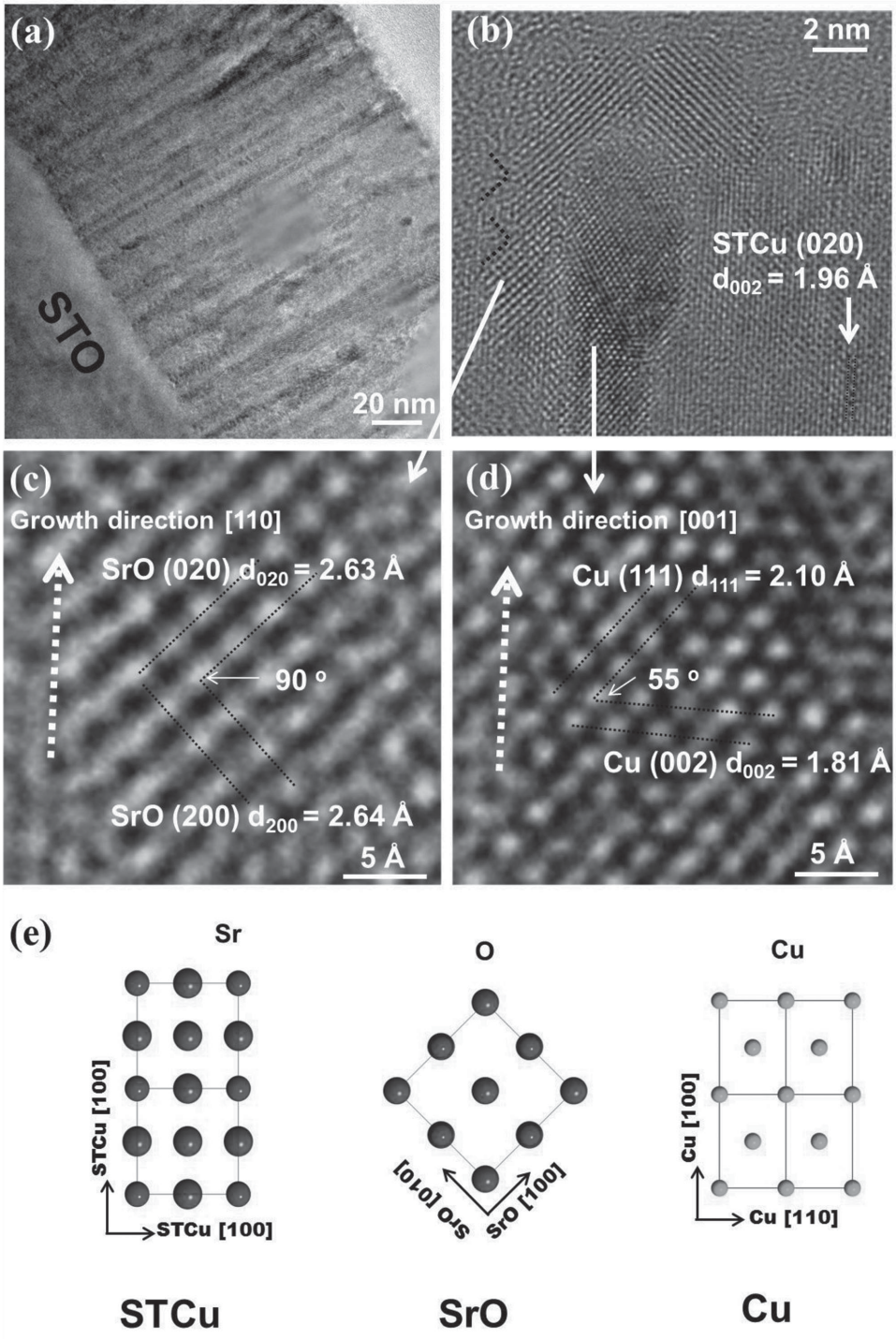

Figure 3. a) Low magnification cross-sectional TEM image of 180 nm thick nc-STCu film grown on STO (001) substrate. b) Magnified cross-sectional TEM image of a Cu nanorod within a SrO pillar after cutting by FIB, imaged along [100] of STO. Magnified TEM images of c) SrO shell and d) Cu core. e) Schematic diagram of the orientation of the lattices of the three phases.

rods appeared to be tilted with respect to the substrate, based on the plan-view images. The projections of the rods on the substrate showed 60° variants on the (111) STO substrate, and mostly parallel alignment on the (011) STO substrate as expected from the substrate symmetry. On Si with native oxide (Figure S2a,b, Supporting Information) and on CeO_2/YSZ-buffered Si substrates (Figure S2c,d, Supporting Information), the top view SEM images showed a polycrystalline matrix. On etching, nanopores were formed indicating phase separation, but without an ordered epitaxial orientation with the substrate.

Conductive atomic force microscopy (cAFM) was used to characterize the electrical conductivity of the three phase

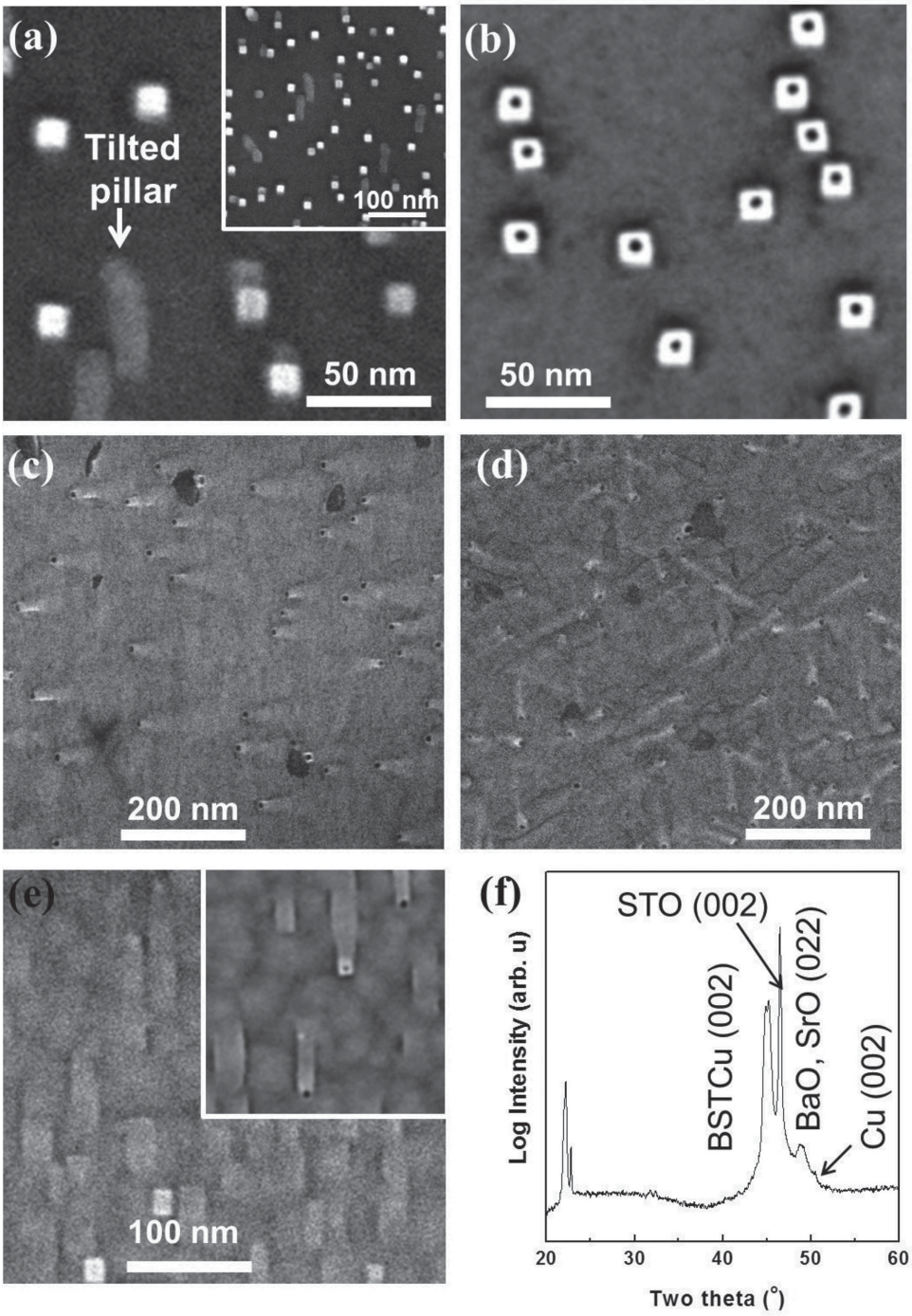

Figure 4. a) Top view SEM images of nc-STCu film grown in vacuum on Nb-doped (001) STO substrate. Inset is a low magnification image showing both vertical and tilted growth of nanorods. b) Top view SEM image of STCu film on Nb-doped STO substrate after etching in ammonium hydroxide for 3 h. Top view SEM images of etched STCu films on c) (011) STO and d) (111) STO substrates. e) Top view SEM and f) XRD pattern of a nanocomposite film grown by combinatorial PLD using BST and CuO targets. Inset in Figure 4e shows a top view SEM image of etched nanocomposite.

nanocomposite on a conductive substrate, Nb-doped (001) STO. The atomic force microscopy (AFM) scan showed larger, rounder pillars than the SEM images due to the finite size of the AFM tip. The expectation was that the SrO pillars would be highly resistive with a conductive Cu core, but the cAFM was unable to resolve the Cu core. However, the scan (Figure S3, Supporting Information) showed that many of the pillars were more conductive than the matrix. This conductivity could arise from the Cu or from interface conduction.

The structural data therefore indicates an epitaxial Cu-SrO-perovskite core–shell-matrix morphology for nc-STCu films grown in vacuum on STO and STO/Si. Figure S4, Supporting

Information, shows that the vertical nanocomposite growth occurred over a temperature range of 500–650 °C, but no phase separation was seen at 700 °C. The low solubility of Cu in $SrTiO_3$ is presumed to have led to the formation of metallic Cu nanorods during growth in vacuum, as seen in other metal/oxide systems.[15–19] The thermodynamic stability curve of Cu in terms of temperature and oxygen partial pressure[38] suggests that Cu becomes stable at an oxygen pressure below 1×10^{-9} Torr at the deposition temperature, 650 °C. (In contrast, when STCu films were grown in 0.1 mTorr of oxygen on STO substrate, a metallic Cu phase was not detected and the out-of-plane lattice parameter was 4.052 ± 0.004 Å suggesting that Cu was present in the STCu lattice.) In the vacuum-deposited films the separation of Cu into metallic rods left the film with excess Sr compared to perovskite, and SrO formed around the Cu with a lattice parameter intermediate between those of STCu and Cu. It was difficult to confirm the presence of SrO with XRD due to overlap with the Cu peak, but a small peak at 49.5° in Figure 1a that remained after etching away the Cu metal may indicate SrO (022). The minimum surface energy of SrO has been reported as being at the (001) planes,[39] therefore, SrO formed microfaceted planes at the interface with STCu as shown in the high resolution TEM image in Figure 3b. There are several reports which discuss the kinetic and thermodynamic factors determining the formation of nanocomposites.[6,13,40–42] Here, we suggest the SrO nanorods form to partially release elastic energy, or as a result of the changes in perovskite composition as the Cu separates out from the matrix phase.

To show another example of the formation of a three-phase system, nanocomposites were also grown by combinatorial PLD by ablating $(Ba_{0.6}Sr_{0.4})TiO_3$ (BST) and CuO targets alternately, with STO (001) as the substrate. A top view SEM image (Figure 4e) and XRD pattern (Figure 4f) of the nanocomposite show the presence of a matrix of perovskite, presumably (Ba,Sr)(Ti,Cu)$O_{3-\delta}$; a BaO or SrO rocksalt phase; and metallic Cu, which could be etched with ammonium hydroxide. This is similar to the nc-STCu morphology, and etching formed holes in the square pillars (inset, Figure 4e). The results confirm the formation of a 3-phase epitaxial system over a limited range of BST:CuO ratios. CuO-rich compositions formed metallic Cu but no rocksalt phase; BST-rich compositions formed rocksalt phase but no Cu. In contrast, nanocomposites grown by combinatorial deposition of STO and CuO did not exhibit the coexistence of SrO and Cu over the composition range studied, but either SrO or Cu were seen.

The nc-STCu provides a chemically and topographically heterogeneous surface, that may be expected to affect the growth of other oxide heterostructures, and possibly even template the growth of other vertical nanocomposites. To investigate this, the growth of a 90 nm thick $BiFeO_3$–$CoFe_2O_4$ (BFO–CFO) nanocomposite on nc-STCu/STO (001) was explored. As a reference, BFO–CFO grown directly on STO (001) showed the expected square or rectangular CFO pillars with edge length of 20–30 nm within a uniform BFO matrix, **Figure 5**a. The epitaxy and electronic properties of such BFO–CFO self-assembled nanocomposites have been widely studied.[5–8] The spinel pillars grew with vertical [110] facets, capped with four (111) tilted facets and a (001) facet at the top of the pillar. However, when the same BFO–CFO nanocomposite was grown on 180 nm thick ammonium hydroxide etched nc-STCu on STO (001), a dramatically different morphology was seen, Figure 5b. The lateral size of the CFO pillars on nc-STCu was much bigger, with edge lengths of 150–200 nm. The inset in Figure 5b indicates the morphology of the nanocomposite after removing the BFO matrix by hydrochloric acid etching for 120 s. A large CFO pillar is seen on top of the finer nc-STCu morphology. Further, some of the CFO pillars on nc-STCu showed a 45°-rotated pillar orientation, indicated by a dashed circle in Figure 5b. We found in previous work that a rough surface promoted multiple pillar orientations,[31] in particular a 45° rotated cube-on-cube epitaxy with CFO [110] · STCu [100] relation. The incidence of 45° rotated pillars is therefore attributed to the roughness of the STCu surface. Within the range of temperatures (≈600–700 °C) suitable to grow the BFO–CFO nanocomposite, there was little temperature-dependence of the morphology or orientation of the CFO pillars.

The BFO–CFO/nc-STCu had a much larger characteristic length than other reported BFO–CFO vertical nanocomposites. The pillar orientations and density are established in the early stages of nanocomposite growth, illustrated by Figure S5, Supporting Information, which shows the initial growth modes of 20 nm thick CFO on STO and nc-STCu/STO substrates. The nc-STCu surface enhanced the surface diffusivity during the nucleation of the CFO pillars. Contact angle measurement with distilled water gave values of 67° on STO and 88° in nc-STCu indicating a difference in surface energy.

Figure 5c,d shows the magnetic hysteresis loops of the BFO–CFO nanocomposite on STO and nc-STCu/STO substrates. The magnetization was calculated for the BFO–CFO layer after removing the background signal from substrate and holder. The BFO–CFO nanocomposite on STO substrate showed a hard magnetic behavior with strong out-of-plane anisotropy as a result of both the elongated pillar shape (height 90 nm, diameter ≈30 nm) and magnetoelastic anisotropy from the out-of-plane compressive strain exerted on the CFO by the BFO. The 10 kOe field of the vibrating sample magnetometer (VSM) was insufficient to saturate the CFO. (Measurements of other BFO–CFO nanocomposites at fields large enough to saturate the magnetization are shown in ref. [31].) On the other hand, the hysteresis loops of the BFO–CFO nanocomposite on nc-STCu showed lower field switching and the out-of-plane anisotropy decreased significantly (Figure 5d).

XRD patterns in Figure 5e,f show the (00*l*) growth of BFO and CFO without secondary phases. For the BFO–CFO/STO, Figure 5e, the out-of-plane lattice parameters were c_{BFO} = 4.031 ± 0.003 Å and c_{CFO} = 8.367 ± 0.002 Å leading to an out-of-plane tensile strain of BFO (ε_{BFO} = 1.017%) and out-of-plane compressive strain of CFO (ε_{CFO} = −0.27%) compared to bulk values ($a_{BFO,bulk}$ = 3.965 Å and $a_{CFO,bulk}$ = 8.390 Å). The predicted anisotropy fields are 1.9 kOe for shape anisotropy and 10.0 kOe for magnetoelastic anisotropy, based on a magnetostriction constant of $\lambda_{100} = -350 \times 10^{-6}$ for CFO, leading to a net H_K = 12 kOe. This is larger than the field applied in the VSM and explains why the loops in Figure 5c are not saturated. The BFO–CFO/nc-STCu/STO, Figure 5f, showed an additional perovskite (002) peak from the STCu matrix and a shift of the BFO and CFO phases towards higher angles. The out-of-plane lattice parameters were c_{STCu} = 3.932 ± 0.002 Å

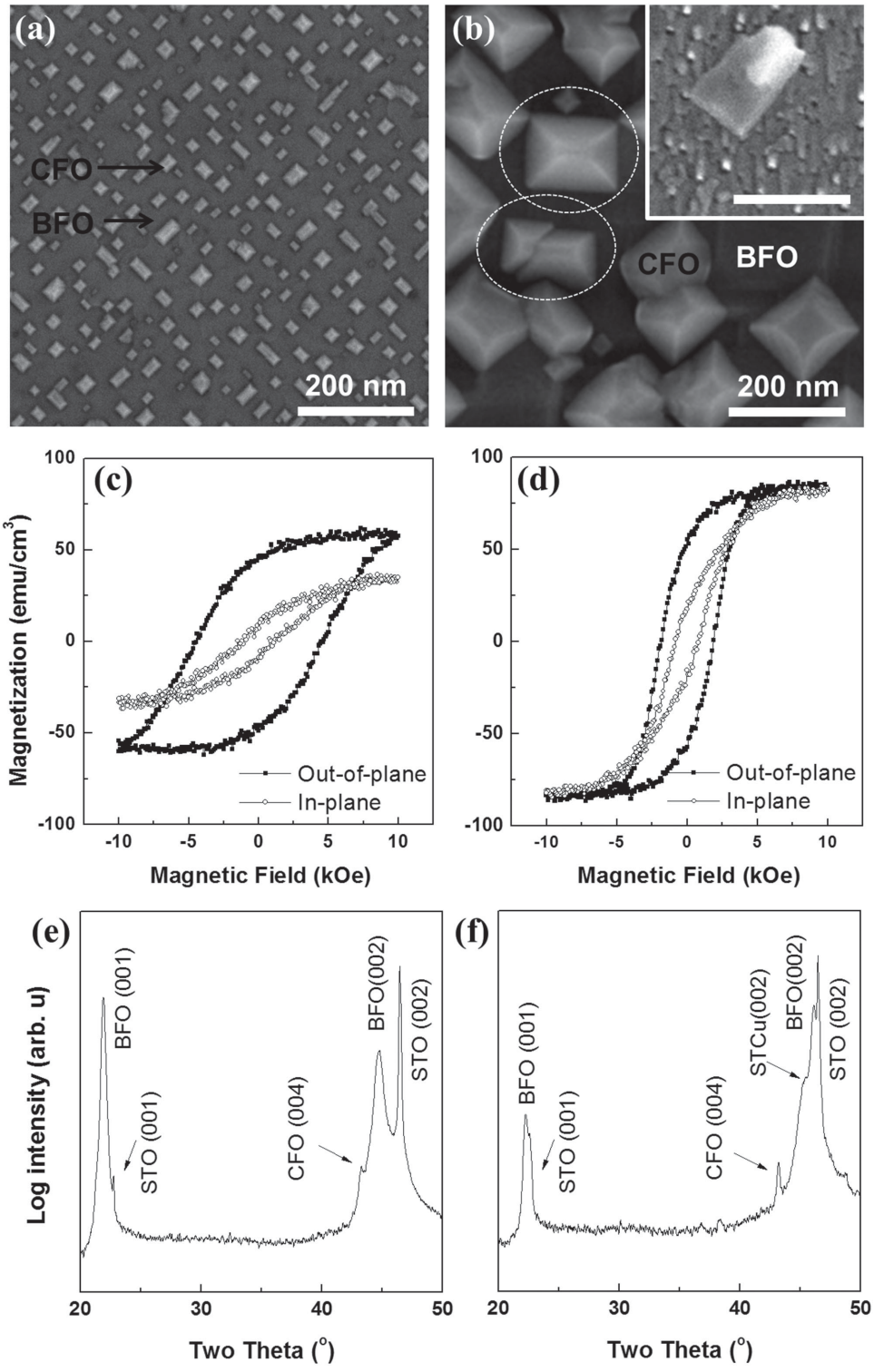

Figure 5. Top view SEM image of 90 nm thick BFO–CFO nanocomposite on a) single crystal (001) STO substrate and b) ammonium hydroxide etched nc-STCu /(001) STO substrate. Inset in (b) is a SEM image of BFO–CFO nanocomposite on STCu/STO substrate after etching in dilute HCl solution for 120 s at room temperature shown with the same magnification as Figure 5b. In-plane and out-of-plane magnetic hysteresis loops of BFO–CFO on c) STO and d) nc-STCu/STO substrate. θ–2θ scans of BFO–CFO on e) STO and f) nc-STCu/STO.

for the STCu perovskite matrix, c_{BFO} = 3.999 ± 0.005 Å and c_{CFO} = 8.370 ± 0.002 Å, giving an out-of-plane strain of ε_{BFO} = 0.9% and ε_{CFO} = –0.23%. In the large, flat CFO crystals shape anisotropy would favor an in-plane easy axis with anisotropy field –2.4 kOe, assuming 150 nm side length, but the magnetoelastic anisotropy favors an out-of-plane easy axis with anisotropy field

8.5 kOe. The net anisotropy field would then be $H_K \approx 6$ kOe which is in reasonable agreement with the hard-axis (in-plane) saturation field, and explains the lower coercivity of the out-of-plane hysteresis loop. Thus the use of an STCu substrate produces large changes in the size, morphology and magnetic properties of an overgrown ferroelectric-ferrimagnetic BFO–CFO nanocomposite, making the STCu an interesting option in the control and integration of these multiferroic nanocomposites.

3. Conclusions

The self-assembly of a three-phase epitaxial perovskite-rock salt-metal nanocomposite thin film of average composition $SrTi_{0.78}Cu_{0.22}O_{3-\delta}$ was demonstrated by pulsed laser deposition of films in vacuum on (001), (011), and (111) oriented $SrTiO_3$, Nb:$SrTiO_3$, and on Si coated with an 8 nm thick epitaxial $SrTiO_3$ film. The resulting films, up to ≈200 nm thick, consisted of a perovskite matrix $Sr(Ti,Cu)O_{3-\delta}$ containing vertical nanorods of SrO with spacings of 10–20 nm and diameters ≈10 nm with a square cross-section. Metallic copper rods with ≈3 nm diameter grew in the center of the SrO nanorods. Nanocomposite formation is attributed to the limited solubility of the Cu in the perovskite matrix and the deposition in vacuum, which led to metallic Cu formation with excess Sr forming SrO around the Cu. Etching of the Cu by ammonium hydroxide created uniform size nanopores. The surface energy and morphology of nc-STCu differ from those of STO, which modified the growth of a BFO–CFO nanocomposite upper layer, producing CFO pillars with larger dimensions and lower magnetic anisotropy compared to BFO–CFO/STO.

Two-phase epitaxial nanocomposites such as spinel-perovskite have already shown a wealth of interesting properties such as strain-mediated multiferroicity, and three-phase epitaxial nanocomposites could enable even greater combinations and cross-coupling of useful properties.

4. Experimental Section

The PLD target was made from powders with weight fractions corresponding to a $SrTi_{0.75}Cu_{0.25}O_3$ composition and was prepared by a conventional oxide sintering process. Detailed target preparation methods were given previously.[35] The target mainly consisted of perovskite $Sr(Ti,Cu)O_3$ (lattice parameter = 3.906 Å) and $Sr_4Ti_3O_4$ with minor phases of $SrCuO_3$ and CuO. Because the solubility of Cu in bulk STO is very low (≈1%) most of the Cu was assumed present in the minor phases.[43]

Films were grown on single crystal (001), (011), and (111) oriented STO, Nb-doped STO, STO-coated Si, and Si substrates by PLD using a KrF excimer laser at substrate temperature of 500–700 °C in a vacuum lower than 2×10^{-6} Torr. The laser energy was 400 mJ per pulse and the fluence at the target was 2.6 J cm^{-2}. Ceramic targets were ablated with 10 Hz of frequency at 8 cm target-substrate distance. The STO-coated Si consisted of an epitaxial 8 nm thick STO layer prepared by molecular beam epitaxy (MBE) after removing the native silicon oxide layer.[31,44] The STO growth procedure was monitored in situ using reflection high energy electron diffraction. The resulting STO film had 1 nm surface roughness. The nc-STCu films had average composition $SrTi_{0.78}Cu_{0.22}O_{3-\delta}$ in which the Ti:Cu ratios were confirmed using wavelength dispersive X-ray spectroscopy (WDS). The Sr shows a slight excess as found in films grown on ceria-buffered Si.[35] Buffered Si substrates were also used.[35]

The metallic Cu was removed by an ammonium hydroxide-based solution as used in copper chemical–mechanical polishing applications.[45] Samples were etched with ammonium hydroxide for three hours at room temperature. We confirmed that both metallic Cu film grown by sputtering on a Si substrate and CuO_2 powder etched well in the ammonium hydroxide solution while CuO powder etched more slowly.

Additional films were grown by combinatorial PLD from two different targets. These films included codeposited $(Ba,Sr)TiO_3$ and CuO (BSTO–CuO), and codeposited $BiFeO_3$ and $CoFeO_4$ (BFO–CFO). The BSTO–CuO films were 100 nm thick and were grown on STO (001) substrates by alternating ablation of BSTO and CuO targets at 2×10^{-6} Torr and 600 °C. The BFO–CFO nanocomposites were 90 nm thick and were grown on STCu/STO samples or directly on STO by alternating ablation of CFO and BFO targets at 5 mTorr and 650 °C. The BFO–CFO nanocomposite was etched with diluted hydrochloric acid (HCl) to remove the BFO phase and reveal the CFO morphology. Detailed film growth and etching processes are described elsewhere.[31,46]

The crystal structure of the films was investigated by X-ray diffractometer (XRD, PANalytical X'Pert Pro). The top view morphology was characterized by scanning electron microscopy (SEM, Helios Nanolab 600). The nanocomposite morphology was investigated using high resolution transmission electron microscopy (HRTEM, JEOL 2010F). TEM sample were prepared with a focused ion beam (FIB) cutting after depositing carbon and Pt to reduce damage from the high energy ion beam.

The chemical bonding and valence states of Sr, Ti, Cu, and O were measured by X-ray photoelectron spectroscopy (XPS, Kratos AXIS Ultra imaging spectrometer with a monochromatic Al Kα radiation source). The binding energies were calibrated from the carbon 1s peak at 285.0 eV. Conductivity measurements of Cu nanorods in nanocomposite films on Nb-doped STO substrates were performed with conductive atomic force microscopy (Veeco Metrology Nanoscope V Scanned Probe Microscope Controller with Dimension 3100 SPM). The magnetic properties of BFO–CFO nanocomposites on nc-STCu films were investigated by vibrating sample magnetometer (VSM) in the range of −10 kOe to 10 kOe magnetic field at room temperature.

Supporting Information

Supporting Information is available from the Wiley Online Library or from the author.

Acknowledgements

The authors gratefully acknowledge FAME, a STARnet Center of SRC supported by MARCO and DARPA, and the National Science Foundation DMR1104912, DMR1309868, and DMR1419807, an NSF MRSEC.

Received: January 26, 2015
Revised: March 6, 2015
Published online: April 10, 2015

[1] J. G. Bednorz, K. A. Müller, *Angew. Chem. Int. Ed.* **1988**, *27*, 735.
[2] S. Jin, T. H. Tiefel, M. McCormack, R. A. Fastnacht, R. Ramesh, L. H. Chen, *Science* **2004**, *303*, 661.
[3] X. Bohigas, J. Tejada, E. del Barco, X. X. Zhang, M. sales, *Appl. Phys. Lett.* **1998**, *73*, 390.
[4] G. Zhao, K. Conder, H. Keller, K. A. Müller, *Nature* **1996**, *381*, 676.

[5] H. Zheng, J. Wang, S. E. Lofland, Z. Ma, L. Mohaddes-Ardabili, T. Zhao, L. Salamanca-Riba, S. R. Shinda, S. B. Ogale, F. Bai, D. Viehland, Y. Jia, D. G. Schlom, M. Wuttig, A. Roytburd, R. Ramesh, *Science* **2004**, *303*, 661.
[6] J. L. MacManus-Driscoll, *Adv. Funct. Mater.* **2010**, *20*, 2035.
[7] Z. Wang, Y. Li, R. Viswan, B. Hu, V. G. Harris, J. Li, D. Viehland, *ACS Nano* **2013**, *7*, 3447.
[8] R. Comes, M. Khokhlov, H. Liu, J. Lu, S. A. Wolf, *J. Appl. Phys.* **2012**, *111*, 07D914.
[9] A. Chen, M. Weigand, Z. Bi, W. Zhang, X. Lu, P. Dowden, J. L. MacManus-Driscoll, H. Wang, Q. Jia, *Sci. Rep.* **2014**, *4*, 5426.
[10] Y.-H. Hsieh, J.-M. Liou, B.-C. Huang, C.-W. Liang, Q. He, Q. Zhan, Y.-P. Chiu, Y.-C. Chen, Y.-H. Chu, *Adv. Mater.* **2012**, *24*, 4564.
[11] A. Chen, Z. Bi, Q. Zia, J. L. MacManus-Driscoll, H. Wang, *Acta Mater.* **2013**, *61*, 2783.
[12] N. M. Aimon, H. K. Choi, X. Y. Sun, D. H. Kim, C. A. Ross, *Adv. Mater.* **2014**, *26*, 3063.
[13] R. Comes, H. Liu, M. Khokhlov, R. Kasica, J. Lu, S. A. Wolf, *Nano Lett.* **2012**, *12*, 2367.
[14] S. M. Stratulat, X. Lu, A. Morelli, D. Hesse, W. Erfurth, M. Alexe, *Nano Lett.* **2013**, *13*, 3884.
[15] F. J. Bonilla, A. Novikova, F. Vidal, Y. Zheng, E. Fonda, D. Demaille, V. Schuler, A. Coati, A. Vlad, Y. Garreau, M. S. Simkin, Y. Dumont, S. Hidki, V. Etgens, *ACS Nano* **2013**, *7*, 4022.
[16] J. Shin, A. Goyal, C. Cantoni, J. W. Sinclair, J. R. Thompson, *Nanotechnology* **2012**, *23*, 155602.
[17] F. Vidal, Y. Zheng, P. Schio, F. J. Bonilla, M. Barturen, J. Milano, D. Demaille, E. Fonda, A. J. A. de Oliveira, V. H. Etgens, *Phys. Rev. Lett.* **2012**, *109*, 117205.
[18] Y. Xin, J. Lu, P. A. Stampe, R. J. Kennedy, *Appl. Phys. Lett.* **2006**, *88*, 112512.
[19] L. Mohaddes, H. Zheng, S. B. Ogale, B. Hannoyer, W. Tian, J. Wang, S. E. Lofland, S. R. Shinde, T. Zhao, Y. Jia, L. Salamanca,-Riba, D. G. Schlom, M. Wuttig, R. Ramesh, *Nat. Mater.* **2004**, *3*, 533.
[20] Z. Ghadyani, M. Kildemo, L. M. S. Aas, Y. Cohin, E. Søndergård, *Opt. Express* **2013**, *21*, 30796.
[21] E. Mugnier, I. Pasquet, A. Barnabé, L. Presmanes, C. Bonningue, P. Tailhades, *Thin Solid Films* **2005**, *493*, 49.
[22] P. L. Taberna, S. Mitra, P. Poizot, P. Simon, J.-M. Tarascon, *Nat. Mater.* **2006**, *5*, 567.
[23] S. W. Tay, L. Hong, Z. Liu, *J. Appl. Phys.* **2005**, *98*, 124308.
[24] S. W. Tay, L. Hong, Z. Liu, *Mater. Chem. Phys.* **2006**, *100*, 60.
[25] Y. Chen, W. Jung, Z. Cai, J. J. Kim, H. L. Tuller, B. Yildiz, *Energy Environ. Sci.* **2012**, *5*, 7979.
[26] P. Abellán, C. Moreno, F. Sandiumenge, X. Obradors, M.-J. Casanove, *Appl. Phys. Lett.* **2011**, *98*, 041903.
[27] W. Lee, J. W. Han, Y. Chen, Z. Cai, B. Yildiz, *J. Am. Ceram. Soc.* **2013**, *135*, 7909.
[28] Y. He, C. Brown, Y. He, J. Fan, C. A. Lundgren, Y. Zhao, *Chem. Commun.* **2012**, *48*, 7741.
[29] K. Peng, Y. Wu, H. Fang, X. Zhong, Y. Xu, J. Zhu, *Angew. Chem. Int. Ed.* **2005**, *44*, 2737.
[30] Z. Huang, N. Geyer, P. Werner, J. de Boor, U. Gösele, *Adv. Mater.* **2011**, *23*, 285.
[31] D. H. Kim, N. M. Aimon, X. Y. Sun, L. Kornblum, F. J. Walker, C. H. Ahn, C. A. Ross, *Adv. Funct. Mater.* **2014**, *24*, 5889.
[32] R. D. Shannon, *Acta Crystallogr* **1976**, *A32*, 751.
[33] C. D. Wagner, W. M. Riggs, L. E. Davis, J. F. Moulder, G. E. Muilenberg, *Handbooks of X-ray Photoelectron Spectroscopy*, Perkin-Elmer Corporation, Minnesota **1978**, pp. 82–83.
[34] I. Lyubinetsky, S. Thevuthasan, D. E. McCready, D. R. Baer, *J. Appl. Phys.* **2003**, *94*, 7926.
[35] D. H. Kim, G. F. Dionne, C. A. Ross, *J. Appl. Phys.* **2013**, *114*, 113902.
[36] J. Padilla, D. Vanderbilt, *Phys. Rev. B* **1997**, *56*, 1625.
[37] T. Sano, D. M. Saylor, G. S. Rohrer, *J. Am. Ceram. Soc.* **2003**, *86*, **1933**.
[38] K. Kim, M. Paranthaman, D. P. Norton, T. Aytug, C. Cantoni, A. A. Gapud, A. Goyal, D. K. Christen, *Supercond. Sci. Technol.* **2006**, *19*, R23.
[39] W. Liu, X. Liu, W. T. Zheng, Q. Jiang, *Surf. Sci.* **2006**, *600*, 257.
[40] X. Obradors, T. Puig, M. Gibert, A. Queraltó, J. Zabaleta, N. Mestres, *Chem. Soc. Rev.* **2014**, *43*, 2200.
[41] C. Moreno, P. Abellán, A. Hassini, A. Ruyter, A. P. del Pino, F. Sandiumenge, M.-J. Casanove, J. Santiso, T. Puig, X. Obradors, *Adv. Func. Mater.* **2009**, *19*, 2139.
[42] R. Zhao, W. Li, J. H. Lee, E. M. Choi, Y. Liang, W. Zhang, R. Tang, H. Wang, Q. Jia, J. L. MacManus-Driscoll, H. Yang, *Adv. Funct. Mater.* **2014**, *24*, 5240.
[43] Y. Ein-Eli, David Starosvetsky, *Electrochimica Acta* **2007**, *52*, 1825.
[44] E. N. Jin, L. Kornblum, D. P. Kumah, K. Zou, C. C. Broadbridge, J. H. Ngai, C. H. Ahn, F. J. Walker, *APL Mater.* **2014**, *2*, 116109.
[45] A. Ayala, T. G. Holesinger, P. G. Clem, V. Matias, Q. X. Jia, H. Wang, S. R. Foltyn, B. Gibbons, *IEEE Trans. Appl. Supercond.* **2005**, *15*, 2703.
[46] D. H. Kim, N. M. Aimon, X. Y. Sun, C. A. Ross, *Adv. Funct. Mater.* **2014**, *24*, 2334.